Electronic Supplementary Information

Atomically Precise $Au_{144}(SR)_{60}$ Nanoclusters (R = Et, Pr) are Capped by Twelve Distinct Ligand Types of 5-fold Equivalence and Display Gigantic Diastereotopic Effects

Tiziano Dainese, Mikhail Agrachev, Sabrina Antonello, Denis Badocco, David M. Black, Alessandro Fortunelli, José A. Gascón, Mauro Stener, Alfonso Venzo, Robert L. Whetten, and Flavio Maran

Table of Contents:

1. Chemicals. Hydrogen tetrachloroaurate trihydrate (Aldrich, 99.9%), tetra-*n*-octylammonium bromide (Aldrich, 98%), ethanethiol (Aldrich, 97%), 1-propanethiol (Aldrich, 99%), sodium borohydride (Aldrich, 99%), tetrahydrofuran (THF, Sigma-Aldrich, 99.9%), toluene (Sigma-Aldrich, 99.7%), diethyl ether (Sigma-Aldrich, 99.8%), methanol (Aldrich, 99.8%), and benzene-d_6 (Aldrich, 99.6%, d_6) were used as received. For electrochemistry, dichloromethane (DCM, VWR, 99.8%) was freshly distilled over CaH_2 and stored under an argon atmosphere. Tetra-*n*-butylammonium hexafluorophosphate (Fluka, 99%) was recrystallized from ethanol. Low conductivity water was milliQ Water pro analysis (Merck). Column chromatography was carried out using silica gel from Macherey-Nagel (MN-Kieselgel 60 M, 230-400 mesh).

2. Synthesis of $Au_{144}(SC_2H_5)_{60}$. A typical synthesis is described for $Au_{144}(SC_2H_5)_{60}$, hereafter $Au_{144}(SC2)_{60}$. 0.50 g (1.27 mmol) of $HAuCl_4 \cdot 3H_2O$ was dissolved in 40 ml THF, and then 0.833 g of tetra-*n*-octylammonium bromide (1.52 mmol, 1.2 equiv) was added. The resulting red solution was stirred for 15 min at 20 °C. The stirring speed was set to 100 rpm and 0.367 ml (5.08 mmol, 4 equiv) of ethanethiol, dissolved in 10 ml of ice-cooled THF (to limit evaporation of the ethanethiol, which boils at 35 °C), was added dropwise over a period of ca. 3 min. The solution quickly became yellow and then, after ca. 45 min, colorless. The stirring speed was increased to 600 rpm, 10 ml of toluene was added, and then a freshly prepared icy-cold aqueous solution (10 ml) of $NaBH_4$ (0.48 g, 12.7 mmol, 10 equiv) was quickly added to the reaction mixture, which was kept at 20 °C. The solution immediately became black and plenty of gas evolved. The reaction progress was monitored by UV-vis absorption spectroscopy. After one day, the reaction mixture was filtered on paper to remove black/dark grey residues insoluble in THF. The filtered solution had a dark-brown color with faint orange hues. THF was removed with a rotary evaporator to leave a black-brownish oily solid covered by a colorless liquid (residual H_2O from aqueous $NaBH_4$). The water phase was removed, and the solid was dissolved in toluene and washed with water (4 x 40 ml) in a separatory funnel. Toluene was evaporated and [*n*-Oct_4N^+][$Au_{25}(SC2)_{18}^-$], which is always present as a by-product of

the reaction, was removed by extraction with acetonitrile to leave $Au_{144}(SC2)_{60}$, as a black residue. The sample was washed a few times first with methanol and then pentane. The so-purified $Au_{144}(SC2)_{60}$ clusters were obtained as a black powder, which was stored at 4 °C. The syntheses of $Au_{144}(SC3)_{60}$ was performed in the same way.

3. Inductively Coupled Plasma Mass Spectrometry. ICP-MS analysis for the determination of the Au and S content was carried out with an Agilent Technologies 7700x ICP-MS (Agilent Technologies International Japan, Ltd., Tokyo, Japan). The instrument was equipped with an octupole collision cell operating in kinetic energy discrimination mode used for the removal of polyatomic interferences and argon-based interferences. Optimal performance was attained by using the collision cell in He mode for gold and He-He mode for sulfur. Operating conditions and data acquisition parameters were as already described.[S1] The ICP-MS was tuned daily using a tuning solution containing 1 µg l^{-1} ^{140}Ce, ^{7}Li, ^{205}Tl, and ^{89}Y (Agilent Technologies, UK). A 100 µg l^{-1} solution (Aristar, BDH, UK) containing ^{115}In, prepared in HNO_3 1.38% was used as internal standard through addition to the sample solution via a T-junction.

For sulfur determination, we used the multielement calibration standard CCS-5 (Inorganic Ventures), which contains 100 µg/mL B, Ge, Hf, Mo, Nb, P, Re, S, Sb, Si, Sn, Ta, Ti, W, Zr in aqueous HF 1.0 % (v/v) and HNO_3 7.14 % (v/v). For gold, we used the multielement calibration standard-3 (Agilent Technologies, UK), which contains 10 µg/mL of Sb, Au, Hf, Ir, Pd, Pt, Rh, Ru, Te, Sn in aqueous 10% HCl/1% HNO_3. Multielement standard solutions for calibration were prepared by gravimetric serial dilution at five different concentrations (S: from 500 µg/L to 1500 µg/L; Au: from 200 µg/L to 1000 µg/L). The solvent used was a 1:3 v/v HNO_3:HCl mixture diluted to 5% with MilliQ water. The parameters of the calibration lines were obtained by using the Theil-Sen nonparametric regression technique.[S2] A Microwave Digestion System (CEM Explorer SP-D Plus) was used for acid digestion. Typically, a 5 mg sample was weighed with 0.01 mg accuracy and digested in 7 g of 1:3 v/v HNO_3:HCl mixture according to the following microwave acid mineralization procedure: ramp temperature from room

temperature to 220 °C in 5 min, then 220 °C for 5 min, pressure 400 PSI, power 300 W. The digestion procedure was repeated 8 times. Each digested solution was diluted on 3 concentration levels and each solution was measured by ICP-MS in 5 times for a total of 120 analyses. Solutions were then diluted with the same solvent used for calibrations.

4. Electrospray Ionization Mass Spectrometry. ESI-MS results were acquired on a Bruker time-of-flight (microTOF) mass spectrometer (Bruker Daltronics), operated in positive mode. All spectra were acquired by direct infusion out of the neat DCM solution of each sample, diluted to a concentration 0.1-mg mL^{-1} (3.0 μM). DCM's high volatility (b.p. = 40 °C) facilitates and simplifies the electrospray process; no co-solvents or electrolyte additives were introduced. Flow rate was 10 μL min^{-1}, and typical data-acquisition times were 0.5 min, such that each spectrum shown consumed ~ 5 μL of solution, containing ~ 0.5 μg or ~ 15 pmol of dry sample. The source was cleaned using neat DCM before and between samples. The mass spectra were externally calibrated[S3] using a commercial sample (nanoComposix gold-dodecanethiolate, nominally 2-nm) that is rich in the Au:SR cluster compositions (144,60), (137,56), and (130,50) spanning an m/z range encompassing the new compounds investigated herein.

The MS parameters were: Mass spectrometer acquisition settings were selected to acquire data from m/z 100 - 40,000, and typically ~ 10,000 spectra were summed per spectrum acquired. Nebulizer pressure was set to 1.5 bar, and nitrogen sheath gas was set to a flow rate of 0.0 L min^{-1} (no flow). The endplate offset and capillary potentials were held at -500 and -5500 V. Capillary exit and skimmer voltage settings were +100 and +33 V. Lens 1 pre-pulse storage and transfer times were 50 μs and 300 μs, respectively. MCP detector voltage was increased to 2350 V (from 2100 V standard) for improved detection of high m/z clusters, *i.e.*, singly-charged (z = 1+) $Au_{144}(SR)_{60}$ compounds in the mass-range near 33-kDa.

5. Nuclear Magnetic Resonance. ^{1}H and ^{13}C NMR spectra were obtained with a Bruker Avance DMX-600 MHz spectrometer equipped with a 5 mm TX-1 triple resonance inverse probe powered by field gradients along the (x,y,z)-axes and operating

at 599.90 and 150.61 MHz, respectively. The probe temperature was controlled within 0.1 °C with a Bruker BVT-3000 temperature controller. Measurements were carried out on 0.5−1 mM solutions of the appropriate cluster in benzene-d_6. Chemical shifts are given in ppm units (δ) downfield from tetramethylsilane used as an internal standard for both ^{1}H and ^{13}C nuclei. To ensure obtaining suitable values for the integrals, a complete relaxation for all the resonances was performed by applying a prescan delay ≥10 s. The proton assignments were carried out by standard chemical shift correlations, correlation spectroscopy (COSY) or total correlation spectroscopy (TOCSY). ^{13}C chemical shifts were assigned through heteronuclear multiple quantum coherence (HMQC) experiments. In this measurement, quadrature along F1 was achieved by using the time-proportional receiver phase incrementation (TPPI) method.

6. Electrochemistry. The cyclic voltammetry (CV) and differential pulse voltammetry (DPV) experiments were carried in a small glass cell containing DCM/0.1 M TBAH, under an Ar atmosphere, and at room temperature. The working electrode was a glassy carbon microdisk (9.10×10^{-4} cm^2), which was prepared by sharpening a 3 mm diameter Tokai GC-20 rod and activated as already described.[S4,S5] The counter electrode was a Pt wire, whereas an Ag wire, which was kept in a tube filled with the same electrolyte solution and separated from the main compartment by a Vycor frit, served as a quasi-reference electrode. All potential values are reported against the KCl saturated calomel electrode (SCE). Calibration of the reference electrode was performed by addition of ferrocene at the end of the experiments; in the solvent/electrolyte system used, the ferricenium/ferrocene redox couple has $E° = 0.460$ V vs SCE. We used a CHI 660c electrochemical workstation. For CV experiments, the feedback correction was applied to minimize the ohmic drop between the working and the reference electrodes. For the DPV experiments, we used peak amplitude of 50 mV, pulse width of 0.05 s, 2 mV increments per cycle, and pulse period of 0.1 s.

7. Electron Paramagnetic Resonance. For continuous-wave electron paramagnetic resonance (cw-EPR) experiments, we used 0.6 mM solutions of $Au_{144}(SC2)_{60}$ and $Au_{144}(SC3)_{60}$ in toluene. The solutions were introduced into 2.8 mm i.d. quartz tubes, degassed by several freeze-pump thaw cycles, and sealed off under vacuum (5×10^{-5} Torr). The samples were then rapidly cooled down to 77 K, and the EPR measurements were carried out in the whole range of temperatures from 5 K up to room temperature. X-band cw-EPR spectra were recorded with a Bruker E580 spectrometer equipped with a dielectric cavity resonator. The temperature was controlled by a helium-flow cryostat system (Oxford CF935) equipped with a variable temperature controller unit (Oxford ITC-4). All experimental data were collected under different microwave conditions (microwave power: P_{MW} = 10 mW; we also tested lower power values). A modulation frequency of 100 kHz and amplitude (peak-to-peak) of 1 G and 5 G were used for all spectra.

8. Computational Details. To confirm the chiral character of the $Au_{144}(SR)_{60}$ structure here utilized as a function of the theory level employed for its description and to investigate its optical response, we performed selected DFT and TDDFT simulations of the structure and the chiroptical spectra of different $Au_{144}(SR)_{60}$ models. The first structure is as in the original $Au_{144}(SH)_{60}$ model.[S6] The second model structure is the $Au_{144}(SCH_3)_{60}$ cluster described in the main text and used as a basis for the NMR simulations. Starting from the original $Au_{144}(SH)_{60}$ model,[S6] a third model structure was generated by replacing H atoms with CH_3 groups, and then subjecting the derived $Au_{144}(SCH_3)_{60}$ configuration to a full geometry optimization using DFT and the Perdew−Burke−Ernzerhof (PBE) exchange-correlation (xc-)functional[S7] with semiempirical Grimme-D3 (zero-damping) dispersion corrections[S8] as implemented in the CP2K code[S9] using GTH pseudopotentials,[S10] a double-zeta-valence-plus polarization basis set, and a cutoff of 400 Rydberg for the auxiliary plane wave representation of the density. For this structural model we also kept the arrangement proposed by Lopez-Acevedo et al.,[S11] in which 2 of the 6 sets of staples equivalent by symmetry, namely two

sets of staples between the poles and the equator of the cluster, exhibit SCH_3 ligands in *cis*-configuration, while the other 4 sets have ligands in *trans*-configuration, as illustrated in Figure S6, left panel. By analyzing this model structure – obtained employing a different DFT approach and details of geometry relaxation – we could confirm that some of the methyl groups of the ligands indeed approach the cluster surface and some H atoms eventually exhibit short H⋯S and H⋯Au distances from S and Au atoms from other staple units, which thus seem to be a feature of this system. We note that our DFT approach uniformly overestimates Au-Au and Au-S distances,[S12] as shown in Table S4 where we compare the distance of these atoms from the center of mass (CM) of the cluster for Str-B[S13] and the structural model we used. However, being uniform this does not affect the difference in dihedral angles between the (CM, Au_{staple}, S) and $(Au_{staple}, S, \alpha\text{-}C)$ planes in our structure (average 64°) with respect to, *e.g.*, Str-B (average 47°), which in turn entails shorter H⋯S contact in our structure (minimum distance: 2.64 Å) with respect to Str-B (minimum distance: 3.12 Å), at the root of the diastereotopic phenomenon observed in this work.

Focusing now on optical response, the optical spectrum of the original $Au_{144}(SH)_{60}$ model was described previously.[S14] Here we simulated the circular dichroism (CD) spectrum of the same cluster, using the ADF suite[S15] and the PBE xc-functional.[S7] The spectrum is in Figure S8. The CD spectrum demonstrates that the non-centrosymmetric arrangement of the $Au_{144}(SH)_{60}$ cluster translates into a strongly chiral optical response (the peaks in rotatory power are ~30 times more intense than in the classic $Au_{38}(SCH_2CH_2Ph)_{24}$ chiral cluster;[S16] this value is indeed significantly large even if one consider that Au_{144} is ca. 4 times the size of Au_{38}. In the simulation of the optical spectrum of the $Au_{144}(SCH_3)_{60}$ we also explored the effect of the *cis/trans* arrangement of the staples. Photo-absorption and CD spectra were calculated for the $Au_{144}(SCH_3)_{60}$ cluster model used in the main text as a basis for the NMR simulations. At variance with the original theoretical structural model,[S11] in our model all staples are in *trans* configuration, as illustrated in the right panel of Figure S6. This model was obtained by freezing the coordinates of the Au atoms to those of the $Au_{144}(SH)_{60}$ model, performing a

local geometry optimization enforcing D5 point group symmetry, and using the ADF program[S15] with PBE xc-functional,[S7] Double Zeta (DZ) basis set, and a charge of 2+. We used the complex polarizability TDDFT method,[S14,S16,S17] the PBE xc-functional for the Kohn-Sham equation while the xc-kernel was approximated according to the Adiabatic Local Density Approximation (ALDA),[S18] a STO basis set of triple-zeta polarized (TZP) quality, and a subset of the ADF STO fitting functions to solve the response equations,[S17] and the Zero Order Regular Approximation (ZORA)[S19] to include relativistic effects (which are crucial for heavy elements such as gold). The photo-absorption spectrum is shown in Figures S9 and S10 and is characterized by a weak feature around 1.3 eV, followed by two shoulders at 2.05 and 2.9 eV, and a maximum at 3.7 eV. The agreement between theory and experiment is qualitatively correct; the deviation of the calculated energy position of the features with respect to the experiment is larger at low energy (0.4 eV), but then it decreases regularly so that the feature found around 3.7 eV is properly described by calculation. The spectra decomposed into Cartesian components follow a similar pattern, due to the spherical shape of the cluster that prevents absorption anisotropy (note that the Z component corresponds to the C_5 rotation axis of the D_5 point group symmetry, therefore the X and Y components are equivalent by symmetry). Figure S11 shows the Rotatory strength (R): below 3 eV three strong positive maxima are calculated at 1.55, 2.20, and 2.75 eV (with R between 1000 and $2000 \cdot 10^{-40}$ $esu^2 cm^2$) while the first negative R is found at 3.35 eV with R = $-1100 \cdot 10^{-40}$ $esu^2 cm^2$. It is worth noting that the partial R contributions are in phase with each other, so they interfere constructively. Overall, the CD spectrum of $Au_{144}(SCH_3)_{60}$ is in tune with that of $Au_{144}(SH)_{60}$ and confirms the intrinsic chirality of the Au-S framework. Again, we note that these values of rotatory strength are very large when compared, at the same level of theory, with the well-characterized chiral $Au_{38}(SC_2H_4Ph)_{24}$ cluster, whose absolute rotatory strength are calculated to remain below $50 \cdot 10^{-40}$ $esu^2 cm^2$ [S16] in the optical energy range (below 3 eV).

9. QM/MM NMR calculations. The QM/MM calculations were carried out with the dispersion corrected functional B3LYP-D3 and basis set 6-31g(d,p) for S, C, and H; and the lanl2dz scalar relativistic pseudo-potential for Au. This level of theory has been previously successful in reproducing NMR experiments in Au_{25} thiolated clusters.[S20] The MM part was taken from our previous parametrization of the AuSBio force field.[S20] The ONIOM method, as implemented in Gaussian 16,[S21] was used for all calculations. The GIAO method was used for the calculation of NMR properties. The structure of $Au_{144}(SCH_3)_{60}$ obtained at the DFT level was used as the framework to calculate chemical shifts. For this purpose we only considered the outer shell of the structure (Figure S12a). Propyl groups were then added to six ligands (2 on the equator and 4 on the pole). All added groups were then energy optimized at the QM/MM level including the patch in Figure S12c as the QM region, while the rest of the system was treated at the MM level. This optimization was carried out freezing all atoms except for the added propyl groups. With the resulting structure we carried out two additional QM/MM calculations for either a polar and equatorial triangle (Figure S12b). Chemical shifts were calculated and recorded for all protons within the propyl groups. Table S3 shows the calculated chemical shifts.
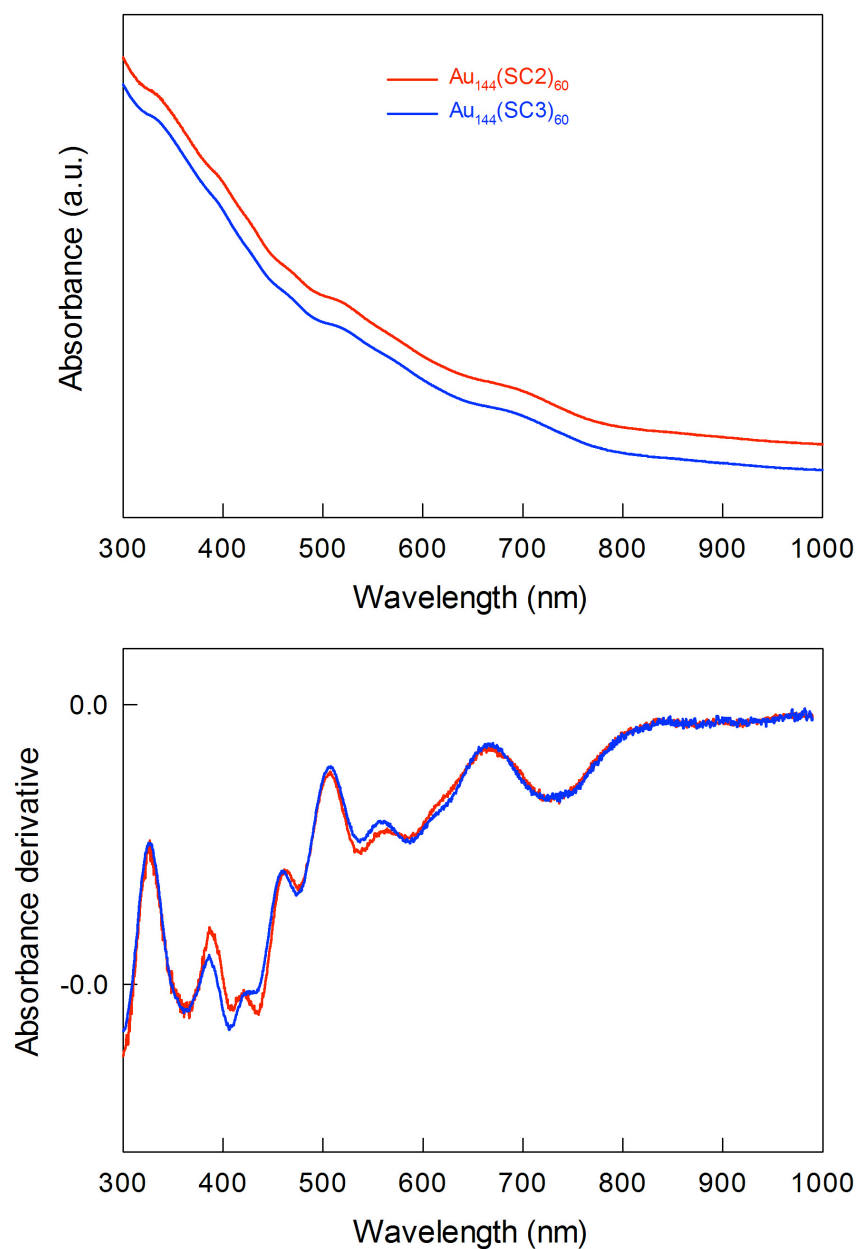
10. Figures S1-S12 and Tables S1-S4.

Figure S1. UV-vis absorption spectra of 0.01 mM $Au_{144}(SCn)_{60}$ in toluene (top graph). The absorption spectrum of $Au_{144}(SC2)_{60}$ has been shifted for clarity. The lower graph shows the corresponding absorption-derivative plots.
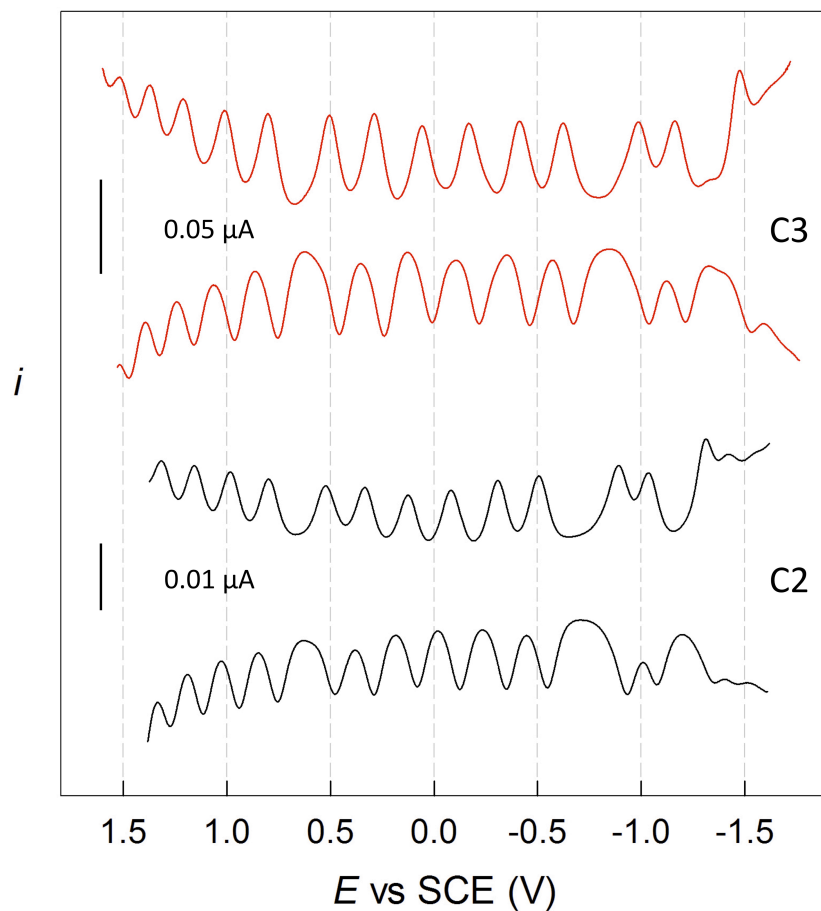
Figure S2. DPV curves for 0.048 mM $Au_{144}(SC2)_{60}$ and 0.19 mM $Au_{144}(SC3)_{60}$ in DCM/0.1 M TBAH at 25 °C on a microdisk glassy-carbon electrode. Both DPVs were obtained with peak amplitude of 50 mV, pulse width of 0.05 s, increments per cycle of 2 mV, and pulse period of 0.1 s.
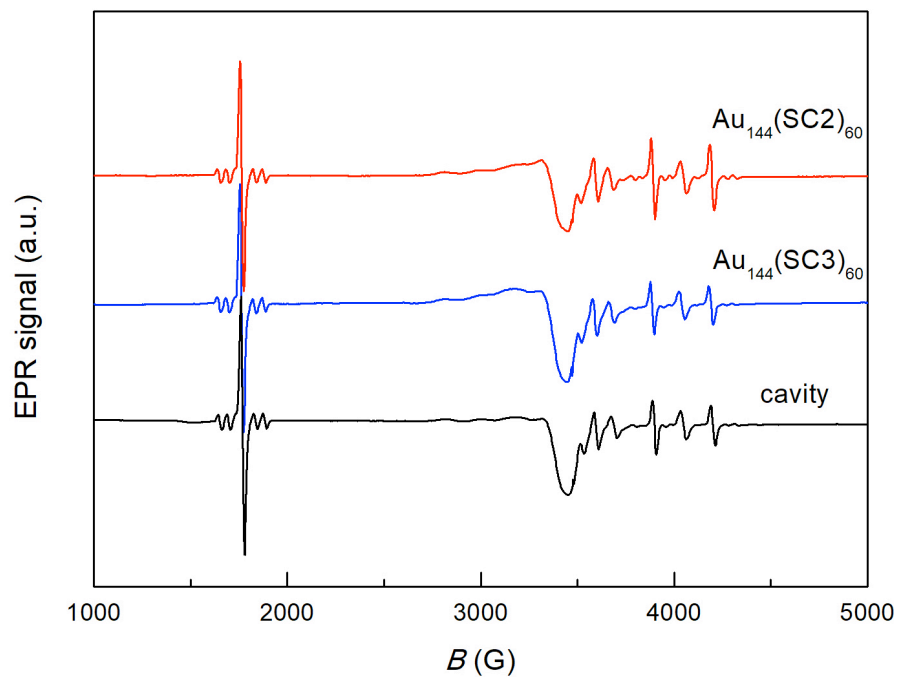
Figure S3. EPR spectra of $Au_{144}(SC2)_{60}$ (red trace) and $Au_{144}(SC3)_{60}$ (blue trace) at 5 K. The black curve shows the reference cavity signal obtained under identical conditions. For the sake of better comparison, the curves have been shifted vertically. Instrumental parameters: microwave frequency of 100 kHz, microwave power of 10 mW, amplitude modulation of 1 G.
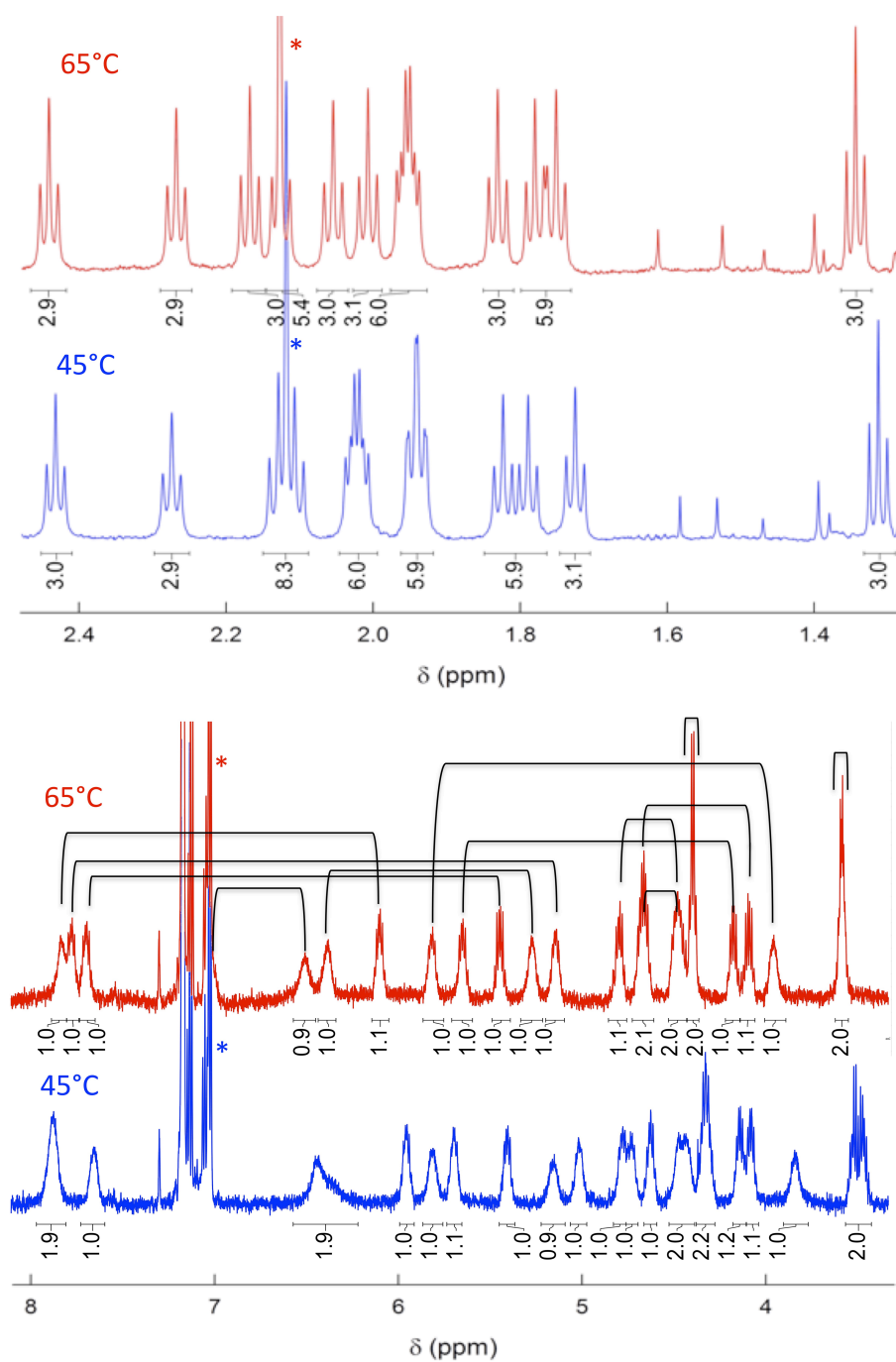
Figure S4. Temperature effect on the ^{1}H NMR spectrum of 1mM $Au_{144}(SC2)_{60}$ in C_6D_6. Integrals are indicated. Top: methyl signals; bottom: methylene signals. In the latter, the scale has been enlarged. The asterisk marks the benzene and/or toluene signals.
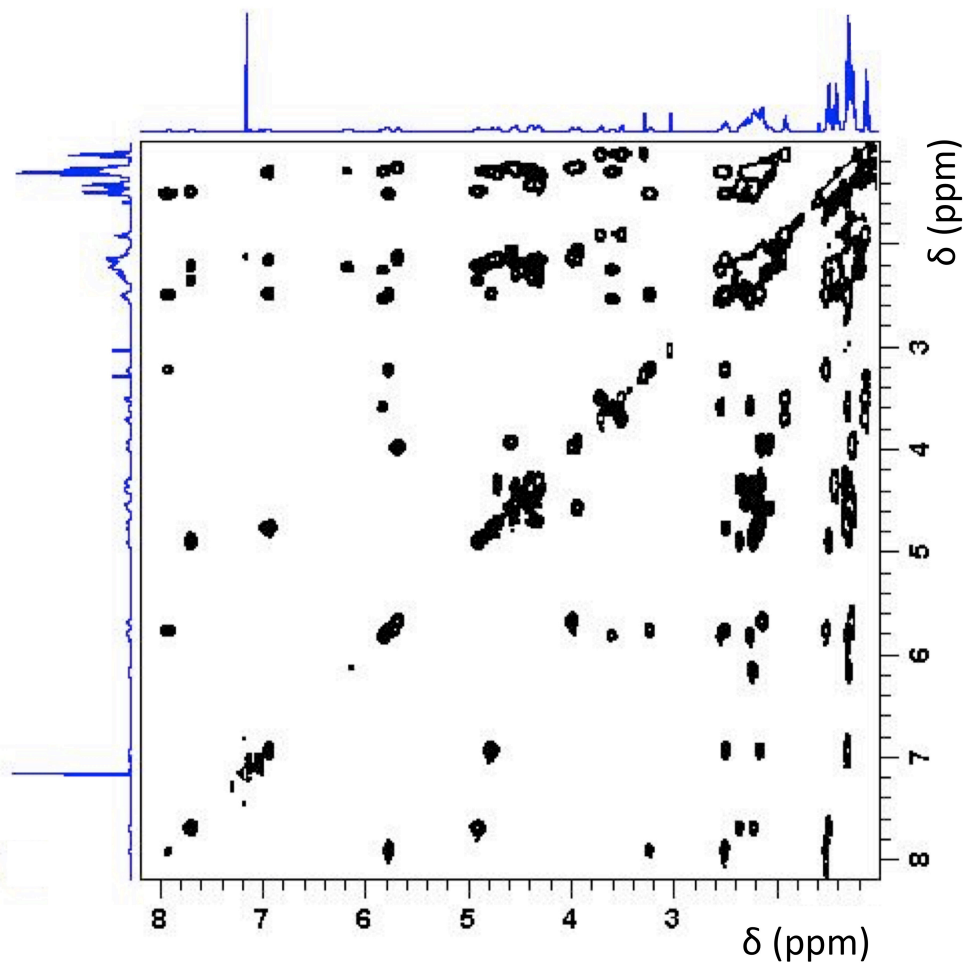
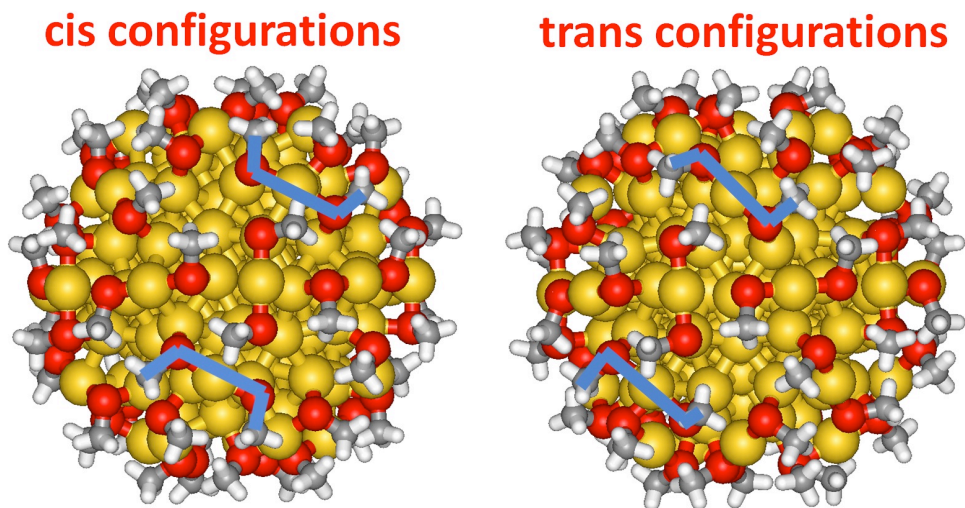Figure S5. TOCSY spectrum of 1 mM $Au_{144}(SC3)_{60}$ in C_6D_6 at 45 °C.

Figure S6. Schematic illustration of the $Au_{144}(SCH_3)_{60}$ cluster as derived from the original $Au_{144}(SH)_{60}$ model and thus exhibiting two sets of staples in the *cis* configuration (left panel) or modified to have all staples in the *trans* configurations (right panel). For clarity, the *cis* or *trans* configurations of two of the staples of each model are highlighted with blue sticks.
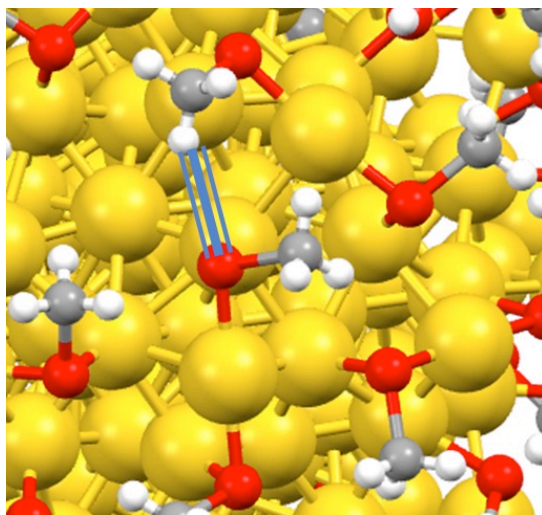
Figure S7. Schematic illustration of a H···S close approach (distance of 2.8 Å) on the locally minimized $Au_{144}(SCH_3)_{60}$ cluster model.
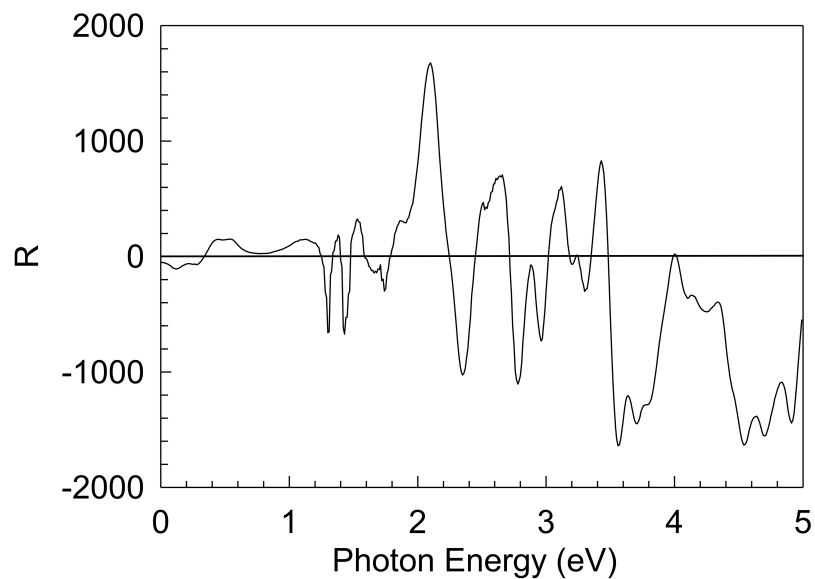
Figure S8. TDDFT Circular Dichroism spectrum of $Au_{144}(SH)_{60}$. Rotatory strength (R) is given in units of 10^{-40} esu^2cm^2.
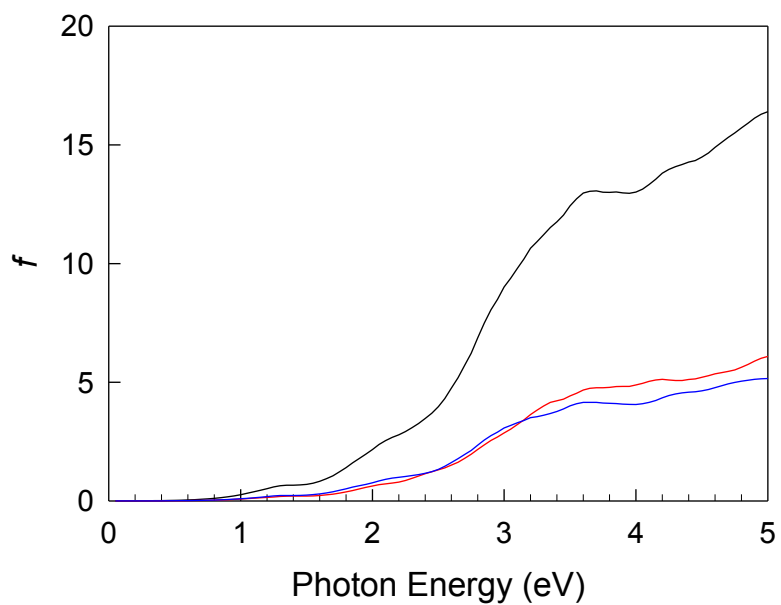
Figure S9. TDDFT photoabsorption spectrum of $Au_{144}(SCH_3)_{60}^{2+}$. Partial contributions are split according to the Cartesian components of the electric dipole, red line: Z component, blue line: X and Y components, black line: total contribution.
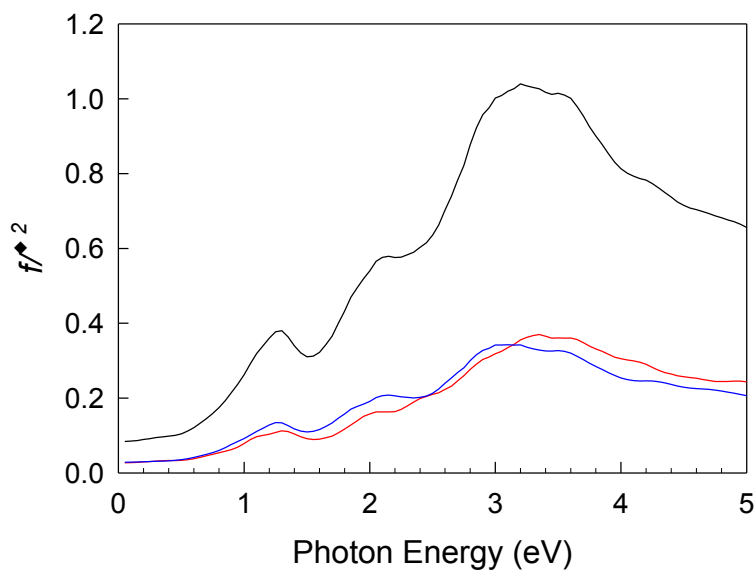
Figure S10. Same as in Figure S9, with the oscillator strength is divided by the square of the photon energy.
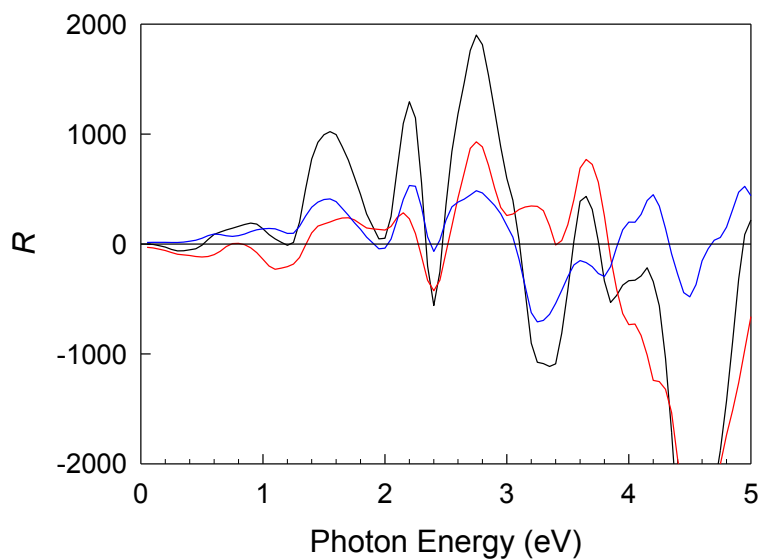
Figure S11. TDDFT Circular Dichroism spectrum of $Au_{144}(SCH_3)_{60}^{2+}$. Partial contributions are split according to the dipole components, red line: Z component, blue line: X and Y components, black line: total contribution. Rotatory strength (R) is given in units of 10^{-40} esu^2 cm^2.

Figure S12. (A) Outer shell used for the QM/MM calculations. (B) QM regions for the calculation of chemical shifts. (C) Description of ligands and characteristic distances involving prominent CH···S contacts.

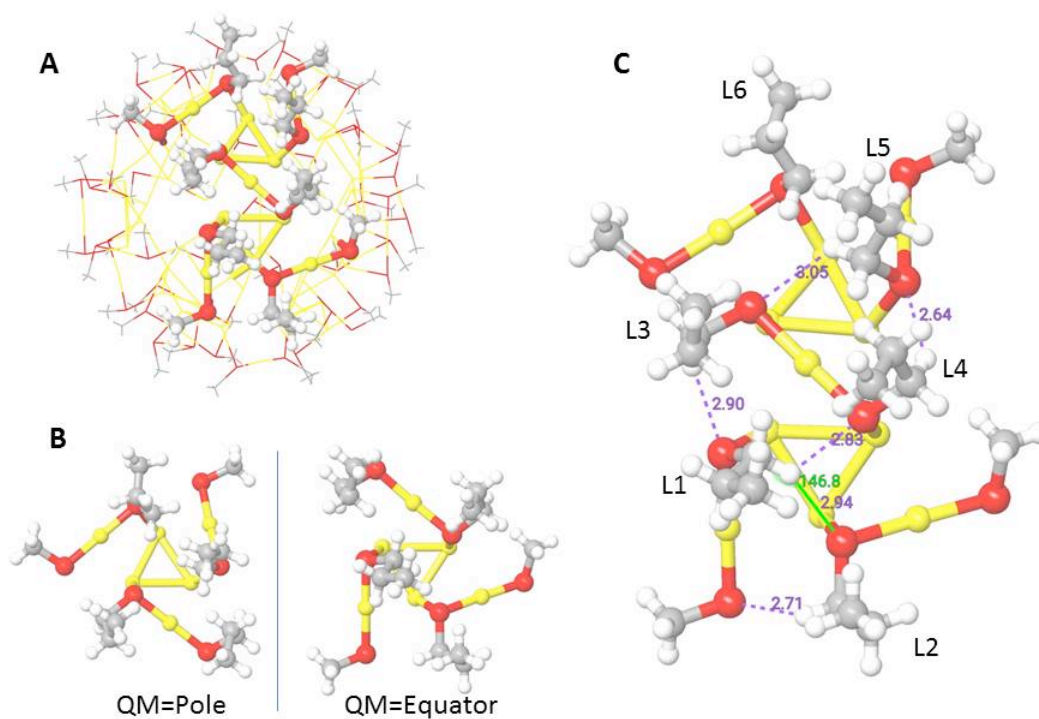| Type	α-CH	Δδ	^{13}C	β-CH	^{13}C
A	3.482	**0.037**	*49.33*	1.314	*24.35*
	3.445				
B	4.748	**0.351**	*34.86*	1.726	*23.01*
	4.397				
C	5.680	**1.567**	*32.81*	1.791	*26.33*
	4.113				
D	4.707	**0.655**	*34.87*	1.826	*23.13*
	4.052				
E	4.603	**0.160**	*34.52*	1.941	*26.23*
	4.443				
F	**7.869**	**2.877**	*34.67*	1.943	*28.75*
	4.992				
G	4.308	**0.030**	*36.83*	2.021	*23.95*
	4.278				
H	6.426	**1.293**	*34.41*	2.028	*31.42*
	5.133				
I	7.076	**0.731**	*38.64*	2.109	*34.82*
	6.345				
J	7.634	**2.245**	*51.32*	2.134	*34.44*
	5.389				
K	5.797	**1.993**	*34.18*	2.276	*32.63*
	3.804				
L	**7.869**	**1.931**	*47.05*	2.433	*28.34*
	5.938				

Table S1. ^{1}H and ^{13}C NMR data for $Au_{144}(SC2)_{60}$ in C_6D_6 at 45 °C. ^{13}C NMR values are in italics, whereas the chemical-shift differences between coupled proton signals (Δδ) are in bold type.

Type	α-CH	Δδ	^{13}C	β-CH	Δδ	^{13}C	γ-CH	^{13}C
A	3.71	**0.20**	*56.0*	1.92	**0.02**	*32.15*	1.12$_6$	*13.58*
	3.51			1.90				
B	4.58	**0.65**	*41.8*	2.14	**0.08**	*33.55*	1.24$_7$	*15.44*
	3.93			2.06				
C	5.68	**1.73**	*40.7*	2.14	**0.02**	*33.58*	1.25$_5$	*15.84*
	3.95			2.12				
D	6.17	**1.31**	*44.8*	2.22	**0.06**	*38.82*	1.27$_7$	*15.68*
	4.86			2.16$_5$				
E	4.57	**0.19**	*42.3*	2.28	**0.06**	*42.32*	1.28$_2$	*15.26*
	4.38			2.21$_6$				
F	6.94	**2.17**	*41.5*	2.48	**0.33**	*43.95*	1.29	*15.27*
	4.77			2.15				
G	4.70	**0.38**	*42.2*	2.30	**0.05**	*32.74*	1.29$_6$	*14.40*
	4.32			2.25				
H	5.81	**2.22**	*58.5*	2.53	**0.29**	*39.78*	1.31	*14.24*
	3.59			2.24				
I	4.39	**0.10**	*40.1*	2.33	**0.13**	*34.25*	1.42$_5$	*15.51*
	4.29			2.19$_7$				
J	7.69	**2.79**	*44.8*	2.35	**0.13**	*35.94*	1.48	*15.10*
	4.90			2.22				
K	7.92	**2.18**	*53.2*	3.21$_3$	**0.72**	*35.59*	1.50$_4$	*16.07*
	5.74			2.49$_1$				
L	3.24	**0.03**	*35.3*	2.50	**0.02**	*35.71*	1.51	*16.00*
	3.21			2.48				

Table S2. ^{1}H and ^{13}C NMR data for $Au_{144}(SC3)_{60}$ in C_6D_6 at 45 °C. ^{13}C NMR values are in italics, whereas the chemical-shift differences between coupled proton signals (Δδ) are in bold type.

	Chemical Shift (ppm)	Δδ (ppm)	Description	
Equator Ligand 1			CH···S Distance	CH···S Angle
CH₃	0.8			
α-CH1	2.9			
α-CH2	4.9	2.0	**2.94 Å**; 2.83 Å	**147°**; 116°
β-CH1	1.4			
β-CH2	1.7	0.3		
Equator Ligand 2				
CH₃	1.2			
α-CH1	6.0			
α-CH2	7.1	1.1	**2.71 Å**	**134°**
β-CH1	2.2			
β-CH2	2.2	0.0		
Pole Ligand 3				
CH₃	0.9			
α-CH1	3.7			
α-CH2	3.6	0.1	2.9 Å	117°
β-CH1	1.7			
β-CH2	1.8	0.1	2.6 Å	118°
Pole Ligand 4				
CH₃	1.2			
α-CH1	2.3			
α-CH2	4.0	1.7	2.64 Å	139°
β-CH1	2.0			
β-CH2	1.3	0.7		
Pole Ligand 5				
CH₃	0.9			
α-CH1	2.9			
α-CH2	4.3	1.4	3.05 Å	125°
β-CH1	1.5			
β-CH2	1.8	0.3		
Pole Ligand 6				
CH₃	1.1			
α-CH1	4.0			
α-CH2	4.2	0.2	3.1 Å	156°
β-CH1	1.8			
β-CH2	1.8	0.0		

Table S3. DFT Calculated δ values, diastereotopic splitting Δδ values, and their geometric fingerprints.

Atom	#	distance-ref.S13	distance-present
Au	12	2.62	2.65-2.67
Au	30	4.72-4.74	4.77-4.84
Au	12	5.54	5.64-5.70
Au	60	6.85-90	6.95-7.10
Au	30	8.68-8.76	8.84-9.14
S	60	8.95-9.11	9.17-9.49

Table S4. Comparison of distances (Å) of Au and S atoms from the center of mass of the cluster in Str-B from Ref. S13 (distance-ref.S13) and in the structural model employed in the simulations discussed in the main text (distance-present). The number of atoms in classes of similar distances is given as "#" in column 2 and the range of values is reported with minimum and maximum values separated by "-".

11. References

S1. D. Badocco, I. Lavagnini, A. Mondin, G. Favaro and P. Pastore, *Spectrochim. Acta Part B*, 2015, **114**, 81-86.

S2. I. Lavagnini, D. Badocco, P. Pastore and F. Magno, *Talanta*, 2011, **87**, 180-188.

S3. D. M. Black, G. Robles, S. B. H. Bach and R. L. Whetten, *Eng. Chem. Res.*, 2018, **57**, 5378-5384.

S4. S. Antonello, M. Musumeci, D. D. M Wayner and F. Maran, *J. Am. Chem. Soc.*, 1997, **119**, 9541-9549.

S5. A. B. Meneses, S. Antonello, M.-C Arévalo and F. Maran, *Electroanalysis*, 2006, **18**, 363-370.

S6. G. Barcaro, L. Sementa, A. Fortunelli and M. Stener, Comment on "(Au–Ag)144(SR)60 alloy nanomolecules" by C. Kumara and A. Dass, Nanoscale, 2011, 3, 3064. *Nanoscale*, 2015, **7**, 8166.

S7. J. P. Perdew, K. Burke and M. Ernzerhof, *Phys. Rev. Lett.*, 1996, **77**, 3865-3868.

S8. S. Grimme, J. Antony, S. Ehrlich and H. A. Krieg, *J. Chem. Phys.*, 2010, **132**, 154104.

S9. J. Hutter, M. Iannuzzi, F. Schiffmann and J. Van de Vondele, *Comp. Mol. Sci.*, 2014, **4**, 15−25.

S10. S. Goedecker, M. Teter, J. Hutter, *Phys. Rev. B: Condens. Matter Mater. Phys.*, 1996, **54**, 1703−1710.

S11. O. Lopez-Acevedo, J. Akola, R. L. Whetten, H. Gronbeck and H. Hakkinen, *J. Phys. Chem. C*, 2009, **113**, 5035−5038.

S12. O. Baseggio, M. De Vetta, G. Fronzoni, D. Toffoli, M. Stener, L. Sementa and A. Fortunelli, *Int. J. Quantum Chem.*, 2018, **118**, e25769.

S13. N. Yan, N. Xia, L. Liao, M. Zhu, F. Jin, R. Jin and Z. Wu, *Sci. Adv.*, 2018, **4**, eaat7259.

S14. O. Baseggio, M. De Vetta, G. Fronzoni, M. Stener and A. Fortunelli, *Int. J. Quantum Chem.*, 2016, **116**, 1603–1611.

S15. E. J. Baerends, D. E. Ellis and P. Ros, *Chem. Phys*., 1973, **2**, 41-51.

S16. O. Baseggio, D. Toffoli, G. Fronzoni, M. Stener, L. Sementa and A. Fortunelli, *J. Phys. Chem. C*, 2016, **120**, 24335-24345.

S17. O. Baseggio, G. Fronzoni and M. Stener, *J. Chem. Phys*., 2015, **143**, 024106.

S18. E. K. U. Gross and W. Kohn, *Adv. Quantum. Chem.*, 1990, **21**, 255-291.

S19. E. V. Lenthe, E. J. Baerends and J. G. Snijders, *J. Chem. Phys.*, 1993, **99**, 4597-4610.

S20. A. Venzo, S. Antonello, J. A. Gascón, I. Guryanov, R. D. Leapman, N. V. Perera, A. Sousa, M. Zamuner, A. Zanella and F. Maran, *Anal. Chem.*, 2011, **83**, 6355–6362.

S21. Gaussian 16, Revision B.01, M. J. Frisch, G. W. Trucks, H. B. Schlegel, G. E. Scuseria, M. A. Robb, J. R. Cheeseman, G. Scalmani, V. Barone, G. A. Petersson, H. Nakatsuji, X. Li, M. Caricato, A. V. Marenich, J. Bloino, B. G. Janesko, R. Gomperts, B. Mennucci, H. P. Hratchian, J. V. Ortiz, A. F. Izmaylov, J. L. Sonnenberg, D. Williams-Young, F. Ding, F. Lipparini, F. Egidi, J. Goings, B. Peng, A. Petrone, T. Henderson, D. Ranasinghe, V. G. Zakrzewski, J. Gao, N. Rega, G. Zheng, W. Liang, M. Hada, M. Ehara, K. Toyota, R. Fukuda, J. Hasegawa, M. Ishida, T. Nakajima, Y. Honda, O. Kitao, H. Nakai, T. Vreven, K. Throssell, J. A. Montgomery Jr., J. E. Peralta, F. Ogliaro, M. J. Bearpark, J. J. Heyd, E. N. Brothers, K. N. Kudin, V. N. Staroverov, T. A. Keith, R. Kobayashi, J. Normand, K. Raghavachari, A. P. Rendell, J. C. Burant, S. S. Iyengar, J. Tomasi, M. Cossi, J. M. Millam, M. Klene, C. Adamo, R. Cammi, J. W. Ochterski, R. L.

Martin, K. Morokuma, O. Farkas, J. B. Foresman and D. J. Fox, Gaussian, Inc., Wallingford CT, 2016.